Halving warming with idealized solar geoengineering moderates key climate hazards

Peter Irvine [1]*, Kerry Emanuel[2], Jie He [3,4,5], Larry W. Horowitz [4], Gabriel Vecchi [6] and David Keith [1]

Solar geoengineering (SG) has the potential to restore average surface temperatures by increasing planetary albedo[1-4], but this could reduce precipitation[5-7]. Thus, although SG might reduce globally aggregated risks, it may increase climate risks for some regions[8-10]. Here, using the high-resolution forecast-oriented low ocean resolution (HiFLOR) model—which resolves tropical cyclones and has an improved representation of present-day precipitation extremes[11,12]—alongside 12 models from the Geoengineering Model Intercomparison Project (GeoMIP), we analyse the fraction of locations that see their local climate change exacerbated or moderated by SG. Rather than restoring temperatures, we assume that SG is applied to halve the warming produced by doubling CO_2 (half-SG). In HiFLOR, half-SG offsets most of the CO_2-induced increase of simulated tropical cyclone intensity. Moreover, neither temperature, water availability, extreme temperature nor extreme precipitation are exacerbated under half-SG when averaged over any Intergovernmental Panel on Climate Change (IPCC) Special Report on Extremes (SREX) region. Indeed, for both extreme precipitation and water availability, less than 0.4% of the ice-free land surface sees exacerbation. Thus, while concerns about the inequality of solar geoengineering impacts are appropriate, the quantitative extent of inequality may be overstated[13].

The idea that an engineered increase in planetary albedo might offset greenhouse gas (GHG)-driven warming is more than half a century old[1]. Early studies addressed the technology and its policy implications[2-4], yet it was not until 2000 that a climate model was first used to study the spatial pattern of the climate response to SG[7]. Since then, at least 100 papers, including many from GeoMIP, have addressed the climate response to various SG scenarios[12,14]. Some methods of SG could enable the world to keep global-mean temperatures below the 1.5 °C warming threshold[15-17]. But, global temperature targets are proxies for local changes in climate variables that drive impacts. SG might hypothetically reduce global-mean surface temperature while still making most people worse off. Indeed, concerns about the climate's response to SG have focused on regional disparities in climate impacts and reductions in precipitation in particular[13,18].

The policy-relevance of prior analysis of the climate response to SG has been limited by several choices. First, many studies focused only on 2-m air temperature and precipitation; yet without accounting for evaporation, precipitation alone is not an effective proxy for water availability or agricultural productivity[19]. Second, many studies assumed SG was used to substitute for emission cuts by offsetting all GHG-induced warming, substantially reducing the strength of the hydrological cycle[6,7,12], and few existing studies evaluated scenarios where SG complements emissions reductions without offsetting all warming[16,20]. Third, despite concern about the potential for SG to worsen climate impacts in some regions, no previous analysis has estimated the fraction of locations that see local climate change exacerbated by SG, where 'exacerbated' means that the absolute deviation from control is increased by SG.

We analyse the distribution of climate changes resulting from reducing the solar constant to offset roughly half the radiative forcing from a doubling of CO_2. A spatially uniform reflective stratospheric aerosol layer, which could be achieved by adjusting aerosol injection using feedback[21,22], would produce a similar radiative forcing to a solar constant reduction. Even with a uniform distribution, stratospheric sulfate SG will differ from a solar constant reduction in that sulfates heat the lower stratosphere, perturb the ozone layer and increase the ratio of diffuse to direct light[15]. Each of these effects can be reduced by the choice of alternate non-sulfate aerosols, although their side-effects are less well understood because there is no direct natural analogue[23]. We nevertheless choose solar constant reduction as a benchmark because, given the diverse implementations of aerosol processes in models, solar modification allows more direct tests of inter-model differences in the climate response to SG.

We use the Geophysical Fluid Dynamics Laboratory (GFDL) HiFLOR model run at a horizontal resolution of ~25 km (see Methods)[11,24,25]. The model endogenously generates tropical cyclones with up to category 5 intensity and substantially reduces biases in regional temperature and precipitation extremes of the current climate compared to lower resolution versions of its model family[11,24]. Relative to a present-day control experiment, we compare the climate response over a 100-year period of an experiment in which CO_2 is doubled (2×CO_2 experiment) to that of an experiment in which the solar constant is reduced by 1% to approximately offset half of the warming from the CO_2 doubling (half-SG experiment, see Methods). We test the robustness of the HiFLOR results by comparing them to those of 12 climate models that participated in the GeoMIP G1 experiment[12,26], in which the global-mean temperature response to an instantaneous quadrupling of CO_2 concentrations is fully offset using a model-dependent reduction in solar constant of roughly 4%. We generate a synthetic half-SG scenario

[1]John A. Paulson School of Engineering and Applied Sciences, Harvard University, Cambridge, MA, USA. [2]Lorenz Center, Massachusetts Institute of Technology, Cambridge, MA, USA. [3]The Program in Atmospheric and Oceanic Sciences, Princeton University, Princeton, NJ, USA. [4]National Oceanic and Atmospheric Administration, Geophysical Fluid Dynamics Laboratory, Princeton, NJ, USA. [5]School of Earth and Atmospheric Sciences, Georgia Institute of Technology, Atlanta, GA, USA. [6]Department of Geosciences and the Princeton Environmental Institute, Princeton University, Princeton, NJ, USA. *e-mail: Peter_irvine@fas.harvard.edu
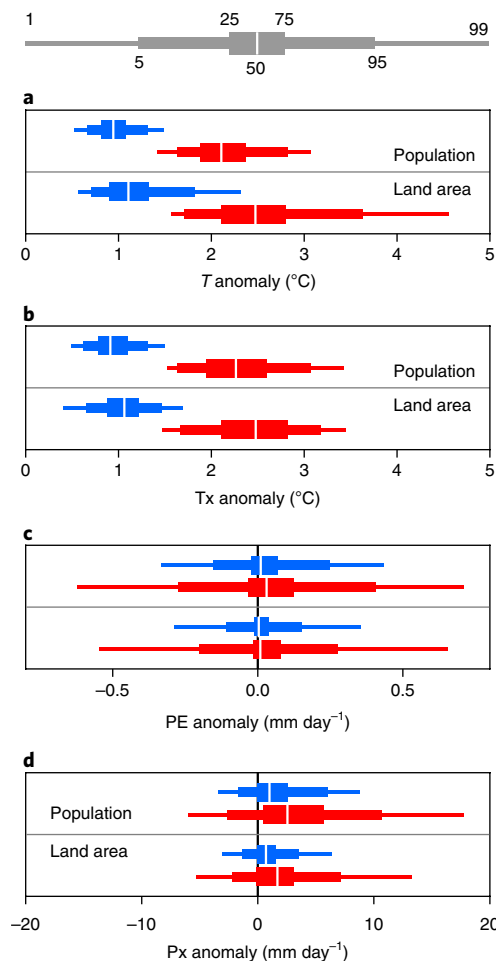
Fig. 1 | The distribution of 2×CO2 and half-SG anomalies by land area and population. a–d, The distribution of 2×CO2 (red) and half-SG (blue) anomalies versus control for the HiFLOR model are shown for surface air temperature (*T*, **a**), maximum annual *T* (Tx, **b**), precipitation–evaporation (PE, **c**), maximum annual 5-day precipitation (Px, **d**). Results are weighted by land area (bottom), excluding Greenland and Antarctica, and by population (top). The legend at the top illustrates how the percentiles of the distribution are shown.

Table 1 | The fraction of the land surface that sees the effects of 2×CO2 (relative to control) significantly exacerbated or moderated by half-SG

	Fraction Exacerbated				Fraction Moderated			
	HiFLOR	GeoMIP			HiFLOR	GeoMIP		
		Med	Min	Max		Med	Min	Max
T	0.0 %	0.0 %	0.0 %	0.0 %	100.0 %	100.0 %	99.2 %	100.0 %
Tx	0.0 %	0.0 %	0.0 %	0.3 %	100.0 %	100.0 %	98.9 %	100.0 %
PE	0.4 %	1.9 %	0.3 %	4.8 %	26.4 %	29.6 %	22.3 %	65.9 %
Px	0.4 %	0.8 %	0.1 %	7.3 %	41.6 %	44.9 %	28.2 %	60.9 %

The percentage of the land area (excluding Greenland and Antarctica) experiencing a statistically significantly greater (exacerbated) or lesser (moderated) absolute magnitude of anomaly for half-SG compared to 2×CO2 (see Methods). Median, minimum and maximum for GeoMIP are calculated across the ensemble of individual model results.

Half-SG also reduces the fraction of land surface that sees substantial drying as measured by a decrease in PE. Under 2×CO2, 3.7% of land surface sees a reduction of PE by more than 0.25 mm day^{-1}, whereas only 1.4% see the same drying under half-SG. The substantial reduction in the magnitude of both positive and negative anomalies shown in Fig. 1 holds for the synthetic half-SG GeoMIP results, for percentage change and standard deviation normalized anomalies, and for precipitation (Supplementary Figs. 1–3).

Why is the spread of the anomalies—for example, the 5–95% range in Fig. 1—smaller under half-SG than 2×CO2? First, half-SG halves the net forcing resulting in an approximately proportional reduction in regional anomalies, reducing the absolute difference between the largest positive and negative anomalies. Second, although not explored here, it is plausible that by reducing the strength of the hydrological cycle and the pole-to-equator temperature gradient, SG reduces two important contributors to temporal climate variability and thereby reduces the variance of time-mean anomalies over our 100-year averaging period.

Which regions are made worse off? Half-SG reduces the fraction of the land area experiencing extreme climatic changes (Fig. 1), but that does not tell us what fraction of points see their climate made worse. To test this, we define the effects of climate change as exacerbated if the absolute magnitude of the half-SG anomaly from the control is significantly greater than the 2×CO2 anomaly, and that they are moderated if half-SG significantly reduces the absolute magnitude of the anomaly. If the control climate is assumed to be preferable to a disturbed climate, then exacerbated/moderated implies that the region is worse/better off. But, this will not always be true as some communities may prefer the altered climate. Table 1 shows the fraction of the land surface where half-SG exacerbates or moderates the effects of 2×CO2 computed using a set of 90% *t*-tests applied to the values at each grid-point (see Methods). T and Tx changes are moderated over almost the entire land surface across all models. For PE and Px, the area moderated is far greater than the area exacerbated in the HiFLOR model and the GeoMIP ensemble. But note that many points do not show a significant change (do not pass the *t*-test). Results are similar when weighted by population and if calculated on a seasonal basis, although the fraction exacerbated in each season in HiFLOR is greater for PE and Px at ~1 % (Supplementary Tables 2 and 3). Previous research has shown that full-SG may in some places overcompensate the effects of 2×CO2; for example, reducing the magnitude but changing the sign of a trend[5–8]. We did not, however, see this in the Half-SG results of HiFLOR. That is, we did not find that any locations where half-SG moderates the 2×CO2 anomaly while at the same location the half-SG anomaly is both statistically significant and of opposite sign. Similarly, we find that only a very small fraction of the land surface
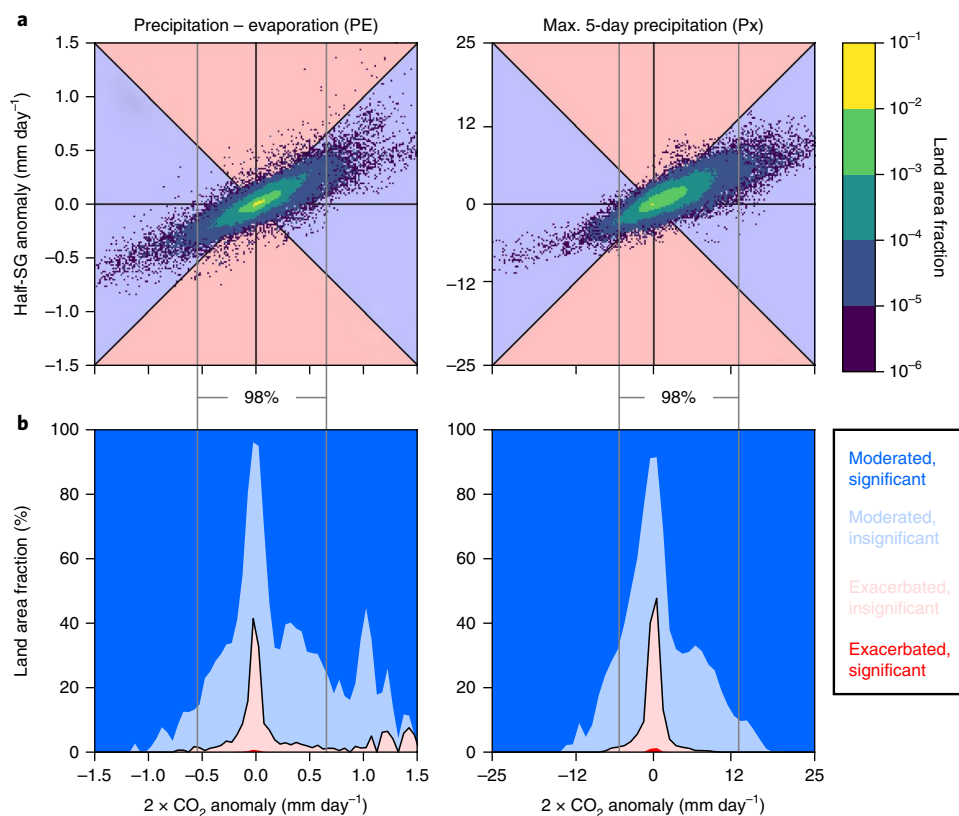
for each of the GeoMIP models by linearly scaling all variables to a value midway between their G1 and 4×CO2 values (see Methods).

We analysed annual means of temperature (T), precipitation minus evaporation (PE), yearly maximum temperature (Tx), yearly maximum precipitation in a 5-day window (Px) and the power dissipation index (PDI) of tropical cyclones (see Methods)[27]. These five variables span most of the drivers of the 'key risks of climate change' identified by the IPCC with the notable exception of sea-level rise (Supplementary Table 1). In contrast to much of the previous literature on SG, we exclude annual-mean precipitation as it is a less effective proxy for water availability than PE (ref. [19]) and a less effective proxy for flood risk than Px (ref. [28]) (although results are included in the Supplementary Information).

Figure 1 shows the distribution of climate changes under 2×CO2 and half-SG versus the control. Since we are focusing on changes relevant to human and terrestrial ecological impacts, we examine land only, excluding Greenland and Antarctica, and compare area-weighted and population-weighed results. It is well known that SG suppresses the hydrological cycle and previous work suggested SG causes drying[5,18,26]. The half-SG scenario reduces the global average precipitation increase from 3.0% under 2×CO2 to 0.5% under half-SG.

Fig. 2 | The joint distribution of 2×CO₂ and half-SG anomalies for HiFLOR with results for the fraction of the land surface where half-SG exacerbates or moderates the climate trend. a,b, Two-dimensional histograms show the distribution of the 2×CO₂ and half-SG anomalies versus control in precipitation–evaporation (PE, **a**) and maximum 5-day precipitation (Px, **b**). The fraction of the land area, excluding Greenland and Antarctica, with anomalies that fall into each bin are indicated by the colour scale, and empty bins are not plotted. To generate the bins for the histograms, the x and y axes are divided into 200 intervals. All points falling closer to the x axis than the diagonal 1:1 lines see the magnitude of the trend reduced (moderated, blue background) by half-SG and all those above and below these lines see the magnitude of the trend increased (exacerbated, pink background). Note that all points, including those that do not see significant change, are plotted. **c,d,** The fraction of the area in which the impacts of 2×CO₂ are exacerbated (red) or moderated (blue) by half-SG as a function of the 2×CO₂ anomaly are shown for PE (**c**) and Px (**d**). Bold colours indicate statistically significant results and pale colours indicate insignificant results. Vertical grey lines show the 1–99% range of 2×CO₂ anomalies.

shows a significant overcompensation and no significant change in magnitude (less than 0.1% for PE).

Figure 2 compares 2×CO₂ and half-SG anomalies (relative to control) of all land points and shows the fraction of points that are exacerbated or moderated as a function of the 2×CO₂ anomaly. Since points with no change under 2×CO₂ cannot see that change reduced, the fraction moderated tends to zero as the 2×CO₂ anomaly tends to zero. Points with the largest anomalies under 2×CO₂ are almost all moderated, while the points that are exacerbated almost all experience very small climatic change; that is, those regions experiencing the greatest climate change are the most likely to see it reduced by half-SG. Similar results are found for precipitation, while T is significantly reduced at all locations (Supplementary Fig. 4).

Only the strongest climate trends are detectable at small spatial scales; to test for weaker, larger-scale trends we aggregate results to the representative climate regions used in the IPCC SREX (see Methods). Figure 3 provides a global overview of the effects of SG on the climate variables assessed here, allowing a qualitative evaluation of whether a region would expect to see aggregate climate risks moderated or exacerbated under half-SG compared to 2×CO₂. None of the four variables are exacerbated (under a 90% t-test) by half-SG in the HiFLOR model in any region. A few regions show PE or Px exacerbated in at least one GeoMIP model, although in only Western South America and South Africa for PE do the number of models

showing an exacerbation exceed the number showing a moderation. Note, however, that in the model regions where half-SG exacerbates change, all had a larger absolute value of PE in half-SG than either 2×CO₂ or control. So, in the few regions where half-SG exacerbates climate change, it increases water availability. This stands in contrast to previous studies and commentary that highlighted concerns that SG would lead to drought[6,10,18]. For Px, in all model regions where half-SG exacerbates change, the absolute value of Px is lower than in either 2×CO₂ or control, indicating less risk of flooding.

Finally, we examined the global intensity of tropical cyclones, including hurricanes and typhoons; directly simulating the tropical cyclone response to SG in a global model for the first time[29,30]. Compared to the control, 2×CO₂ increases the sum of the PDI over all tropical cyclones in HiFLOR by 17.6%. Half-SG offsets most of this, reducing the increase in PDI to 2.4%. As there is currently substantial uncertainty in regional projections of tropical cyclone activity changes[31,32], in this paper we provide only the global results. In addition, we downscaled the HiFLOR output using the technique of Emanuel et al. (2008)[31] to produce 40,000 synthetic cyclones globally in years 100–300 of the control and 2×CO₂ climates, and 26,000 events in years 171–300 of the half-SG climate (see Methods). The downscaled storms show a much weaker response than HiFLOR, with a 5.1% increase in PDI in 2×CO₂ and a 2.0% decrease in half-SG, both relative to the control. This result differs substantially
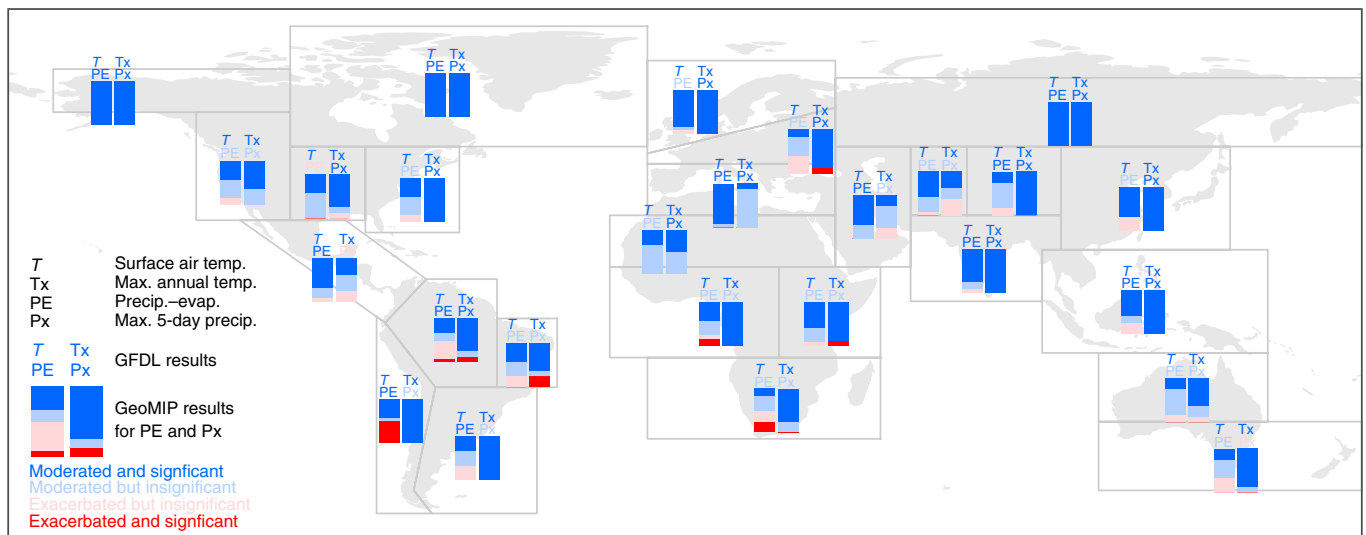
297

Fig. 3 | Regional distribution of where half-SG moderates or exacerbates the absolute magnitude of 2×CO$_2$ anomalies in HiFLOR (for *T*, Tx, PE and Px) and the GeoMIP ensemble (PE and Px). Regions where half-SG moderates (blue) or exacerbates (red) the absolute magnitude of the 2×CO$_2$ climate anomalies relative to control are illustrated. Statistically significant results are indicated with bold colours whereas insignificant results are shown with pale colours (see Methods). The results for the GeoMIP models are shown for precipitation–evaporation (PE, left-column) and Px (right-column) with the columns coloured to indicate the fraction of GeoMIP models with each result. All GeoMIP models show a statistically significant reduction in *T* and Tx in all regions (not shown).

from downscaling Coupled Model Intercomparison Project phase 5 (CMIP5) models for the RCP 8.5 emissions pathway[33], which showed large increases in power dissipation. We speculate that well-resolved tropical cyclones in the fully coupled HiFLOR model may retard changes in monthly mean potential intensity[34], damping the response of synthetic storms to climate change.

We focused on an idealized SG scenario that approximately halves the warming from doubling CO$_2$, and so more-or-less restores the intensity of the hydrological cycle, rather than the typical scenario in which SG offsets all warming. Supplementary Fig. 5 shows how the outcomes change as a function of the level of solar constant reduction and makes clear that beyond offsetting around half of the warming from 2×CO$_2$, the marginal benefits of further cooling decline and the fraction of the land in which climate change is exacerbated grows. While we do not claim that halving warming is necessarily optimal, we suggest it is a better starting point for analysis than a complete offset scenario, as it avoids more-than-reversing many climate trends as happens under scenarios that offset all warming.

It would be premature to conclude from this study that no region would experience greater aggregate climate risks in a real-world deployment of SG that halved anthropogenic warming, as we analysed an idealized scenario and a limited set of climate variables. Our results do not, however, support the common claims that SG would inevitably lead to significant harms to some regions[18], nor the claims that SG's benefits and harms always have a strongly unequal distribution[13].

Online content

Any methods, additional references, Nature Research reporting summaries, source data, statements of data availability and associated accession codes are available at https://doi.org/10.1038/s41558-019-0398-8.

References

1. PSAC *Restoring the Quality of Our Environment* (President's Science Advisory Committee, 1965).
2. Keith, D. W. & Dowlatabadi, H. A serious look at geoengineering. *Eos Trans. Am. Geophys. Union* **73**, 289–292 (1992).
3. Schelling, T. C. in *Changing Climate* (eds Nierenberg, W. A. et al.) (National Academy of Sciences, Washington DC, 1983).
4. Teller, E., Wood, L. & Hyde, R. Global warming and ice ages: I. Prospects for physics-based modulation of global change. *Int. Symp. Planetary E mergencies* vol. 29 (1997).
5. Tilmes, S. et al. The hydrological impact of geoengineering in the Geoengineering Model Intercomparison Project (GeoMIP). *J. Geophys. Res. Atmos.* **118**, 11036–11058 (2013).
6. Lunt, D. J., Ridgwell, A., Valdes, P. J. & Seale, A. 'Sunshade World': a fully coupled GCM evaluation of the climatic impacts of geoengineering. *Geophys. Res. Lett.* **35**, L12710 (2008).
7. Govindasamy, B. & Caldeira, K. Geoengineering Earth's radiation balance to mitigate CO$_2$-induced climate change. *Geophys. Res. Lett.* **27**, 2141–2144 (2000).
8. Irvine, P. J., Ridgwell, A. J. & Lunt, D. J. Assessing the regional disparities in geoengineering impacts. *Geophys. Res. Lett.* **37**, L18702 (2010).
9. Ricke, K. L., Moreno-Cruz, J. B. & Caldeira, K. Strategic incentives for climate geoengineering coalitions to exclude broad participation. *Environ. Res. Lett.* **8**, 014021 (2013).
10. Crook, J., Jackson, L. S., Osprey, S. M. & Forster, P. M. A comparison of temperature and precipitation responses to different earth radiation management geoengineering schemes. *J. Geophys. Res. Atmos.* **120**, 9352–9373 (2015).
11. van der Wiel, K. et al. The resolution dependence of contiguous US precipitation extremes in response to CO$_2$ forcing. *J. Clim.* **29**, 7991–8012 (2016).
12. Kravitz, B. et al. The Geoengineering Model Intercomparison Project (GeoMIP). *Atmospheric Sci. Lett.* **12**, 162–167 (2011).
13. National Research Council. *Climate Intervention: Reflecting Sunlight to Cool Earth* (National Academies Press, Washington DC, 2015).
14. Irvine, P. J., Kravitz, B., Lawrence, M. G. & Muri, H. An overview of the Earth system science of solar geoengineering. *Wiley Interdiscip. Rev. Clim. Change* **6**, 815–833 (2016).
15. Boucher, O. et al. in *Climate Change 2013: The Physical Science Basis* (eds Stocker, T. F. et al.) (Cambridge Uni. Press, Cambridge, 2013).
16. MacMartin, D. G., Ricke, K. L. & Keith, D. W. Solar geoengineering as part of an overall strategy for meeting the 1.5 °C Paris target. *Phil. Trans. R Soc. A* **376**, 20160454 (2018).
17. Jones, A. C. et al. Regional climate impacts of stabilizing global warming at 1.5 K using solar geoengineering. *Earth. Fut.* **6**, 230–251 (2018).
18. Robock, A., Oman, L. & Stenchikov, G. L. Regional climate responses to geoengineering with tropical and Arctic SO$_2$ injections. *J. Geophys. Res. Atmos.* **113**, D16101 (2008).

19. Swann, A. L. S., Hoffman, F. M., Koven, C. D. & Randerson, J. T. Plant responses to increasing CO_2 reduce estimates of climate impacts on drought severity. *Proc. Natl Acad. Sci. USA* **113**, 10019–10024 (2016).
20. MacMartin, D. G., Caldeira, K. & Keith, D. W. Solar geoengineering to limit the rate of temperature change. *Philos. Trans. R. Soc.* **372**, 20140134 (2014).
21. Dai, Z., Weisenstein, D. K. & Keith, D. W. Tailoring meridional and seasonal radiative forcing by sulfate aerosol solar geoengineering. *Geophys. Res. Lett.* **45**, 1030–1039 (2018).
22. Kravitz Ben et al. First simulations of designing stratospheric sulfate aerosol geoengineering to meet multiple simultaneous climate objectives. *J. Geophys. Res. Atmospheres* **122**, 12616–12634 (2018).
23. Keith, D. W., Weisenstein, D. K., Dykema, J. A. & Keutsch, F. N. Stratospheric solar geoengineering without ozone loss. *Proc. Natl Acad. Sci. USA* **113**, 14910–14914 (2016).
24. Murakami, H. et al. Simulation and prediction of category 4 and 5 hurricanes in the high-resolution GFDL HiFLOR coupled climate model. *J. Clim.* **28**, 9058–9079 (2015).
25. Bhatia, K., Vecchi, G., Murakami, H., Underwood, S. & Kossin, J. Projected response of tropical cyclone intensity and intensification in a global climate model. *J. Clim.* **31**, 8281–8303 (2018).
26. Kravitz, B. et al. Climate model response from the Geoengineering Model Intercomparison Project (GeoMIP). *J. Geophys. Res. Atmos.* **118**, 8320–8332 (2013).
27. Emanuel, K. Increasing destructiveness of tropical cyclones over the past 30 years. *Nature* **436**, 686–688 (2005).
28. Curry, C. L. et al. A multi-model examination of climate extremes in an idealized geoengineering experiment. *J. Geophys. Res. Atmospheres* **119**, 3900–3923 (2014).
29. Jones, A. C. et al. Impacts of hemispheric solar geoengineering on tropical cyclone frequency. *Nat. Commun.* **8**, 1382 (2017).
30. Wang, Q., Moore, J. C. & Ji, D. A statistical examination of the effects of stratospheric sulfate geoengineering on tropical storm genesis. *Atmospheric Chem. Phys.* **18**, 9173–9188 (2018).
31. Emanuel, K., Sundararajan, R. & Williams, J. Hurricanes and global warming: results from downscaling IPCC AR4 simulations. *Bull. Am. Meteorol. Soc.* **89**, 347–368 (2008).
32. Walsh, K. J. E. et al. Tropical cyclones and climate change. *Wiley Interdiscip. Rev. Clim. Change* **7**, 65–89 (2016).
33. Emanuel, K. A. Downscaling CMIP5 climate models shows increased tropical cyclone activity over the 21st century. *Proc. Natl Acad. Sci. USA* **110**, 12219–12224 (2013).
34. Emanuel, K. A simple model of multiple climate regimes. *J. Geophys. Res. Atmos.* **107**, ACL 4-1–ACL 4-10 (2002).

Author contributions

P.I., D.K. and G.V. conceived and designed the study. P.I. and D.K. developed the analysis approach. G.V. and L.W.H. performed the HiFLOR simulations and K.E. performed the downscaled tropical cyclone simulations. P.I. and J.H. analysed the main results. K.E. analysed the tropical cyclone results. P.I. and D.K. wrote the paper.

Competing interests

The authors declare no competing interests.

Additional information

Supplementary information is available for this paper at https://doi.org/10.1038/s41558-019-0398-8.

Reprints and permissions information is available at www.nature.com/reprints.

Correspondence and requests for materials should be addressed to P.I.

Journal peer review information: Nature Climate Change thanks Trude Storelvmo, Claudia Timmreck and other anonymous reviewer(s) for their contribution to the peer review of this work.

Publisher's note: Springer Nature remains neutral with regard to jurisdictional claims in published maps and institutional affiliations.

Methods

Models and experiments. *Geophysical Fluid Dynamics Lab (GFDL) HiFLOR.* We employ the GFDL HiFLOR model[24], a higher atmospheric resolution version of the GFDL FLOR model[25,35]. The atmosphere and land components of HiFLOR are taken from the Coupled Model, v.2.5 (CM2.5)[36] developed at GFDL, whereas the ocean and sea ice components are based on the GFDL Coupled Model, v.2.1 (CM2.1)[37–39]. HiFLOR employs a cubed-sphere geometry[40] with a 25-km mesh in the atmosphere and land components, and a 1° latitude-longitude tripolar mesh (with meridional refinement near the equator) for sea ice and ocean components; physical processes and the ocean component were inherited from FLOR (50-km cubed-sphere mesh for atmosphere and land) with only minor changes to the dynamical core and physical parameterizations. In increasing the dynamical core atmospheric resolution, the dynamical time step of the model was halved but the physics time step (time step of the convection, cloud and radiation schemes in the model) was kept the same as in FLOR[24]. The full details of the setup of HiFLOR can be found in Murakami et al.[24].

HiFLOR can simulate tropical cyclones up to category 5, capturing their structure, spatial distribution and interannual variations, and is the first global coupled model that has been able to do this[24]. HiFLOR produces skilled seasonal forecasts of the number of intense tropical cyclones and the number of land-falling tropical cyclones that are better than the earlier FLOR model[41]. HiFLOR is better able to reproduce the observed tropical sea-surface temperature and precipitation climatology that means that it has a more realistic walker circulation and an improved simulation of the tropical cyclone response to the El Nino Southern Oscillation[42]. The higher resolution of HiFLOR (0.25°) compared to FLOR (0.5°), CM2.5 (0.5°) or CM2.1 (2.0°, a resolution typical of GeoMIP and CMIP5 models) allows for a far better simulation of all aspects of observed precipitation extremes in the United States[11]. While a similar mean intensification of precipitation has been found across these model resolutions, HiFLOR predicts a substantial increase in intense precipitation associated with tropical cyclones across the southeast United States that is not captured by the lower resolution model[11].

For GFDL HiFLOR a 300-yr control climate simulation was run with radiative forcing and land-use conditions representative of the year 1990 and initiated with 1990 observations[24]. The fixed forcing agents for the control simulations are atmospheric CO_2, CH_4, N_2O, halons, tropospheric and stratospheric O_3, anthropogenic tropospheric sulfates, black and organic carbon and solar irradiance. The $2\times CO_2$ experiment starts in year 100 of the control simulation with a 1% per year increase in CO_2 concentrations that halts at year 170, the point of doubling, and remains fixed until the end of the simulation in year 300. HiFLOR has an equilibrium climate sensitivity of 2.8 °C and a transient climate response of 1.53 °C. The half-SG simulation begins at year 170 of the $2\times CO_2$ experiment with an instantaneous 1% reduction in solar constant and runs until year 300. This experiment is referred to as half-SG as it offsets roughly half of the warming from the $2\times CO_2$ experiment (53%: $2\times CO_2$ is 2.0 °C warmer than control and half-SG 0.93 °C warmer). The last 100 years of the experiments are used for the averaging period. A single member was run for each experiment.

GeoMIP. For the GeoMIP ensemble we draw on 12 models from the GeoMIP G1 set of experiments (Supplementary Table 5)[12]. Table 1 of Kravitz et al.[26]. lists the model setups for all GeoMIP models analysed here and provides an overview of the climate response of these models for the GeoMIP G1 experiment. The pre-industrial control experiment is specified as in the CMIP5[43]. The $4\times CO_2$ experiment spins off from the pre-industrial control with an instantaneous quadrupling of CO_2 concentrations. The G1 experiment is the same as the $4\times CO_2$ experiment but with an instantaneous reduction in solar constant chosen to restore the global-mean top-of-atmosphere radiative balance to that of the pre-industrial in so far as possible. This experiment is referred to here as full-SG as it offsets all of the warming from the $4\times CO_2$ experiment. The G1 experiment runs for a total of 50 years and the last 40 years of the experiment are used for the averaging period, the matching 40 years are used as the averaging period for the other two experiments. A single ensemble member is used for each model and experiment.

Downscaled tropical cyclone simulations. The downscaling technique is described in detail by Emanuel et al.[31,44]. The technique begins by randomly seeding with weak hurricane-like disturbances the large-scale, time-evolving state given by the global climate data. These seed disturbances are assumed to move with the large-scale flow in which they are embedded, plus a westward and poleward component owing to planetary curvature and rotation. Their intensity is calculated using a simple, circularly symmetric hurricane model coupled to a very simple upper ocean model to account for the effects of upper ocean mixing of cold water to the surface. Applied to the synthetically generated tracks, this model predicts that a large majority of seed storms dissipate owing to unfavourable environments. Only the 'fittest' storms survive; thus the technique relies on a kind of natural selection. The model is extremely fast and many thousands or tens of thousands of storms can easily be simulated. Extensive comparisons to historical events by Emanuel et al.[31] and subsequent papers provide confidence that the statistical properties of the simulated events are consistent with those of historical tropical cyclones.

Scaling. To produce comparable results to the half-SG experiment of GFDL HiFLOR we scale the results of GeoMIP G1 to estimate the climate response of a solar constant reduction that offsets only half the radiative forcing from the $4\times CO_2$ experiment. The scaled results are calculated as follows

$$X_f = X_{4\times CO_2} + f \times (X_{G1} - X_{4\times CO_2}) \qquad (1)$$

where X is the variable to be scaled and f is the fraction of the $4\times CO_2$ radiative forcing offset (0.5 for half-SG). The scaling is applied not only to the means but also to the standard deviations as well for the purposes of calculating statistical significance. Equation (1) is also used to scale the results of the half-SG GFDL HiFLOR experiment to produce Supplementary Fig. 5.

Previous studies of SG have evaluated the response across a range of scenarios with different radiative forcings finding an approximately linear response to forcing magnitude at the regional level for temperature and precipitation[8,45]. However, some aspects of the response are not linear, for example, Schaller et al.[46] found that the poleward energy transport did not respond linearly to combinations of solar and CO_2 forcing. To test the performance of this linearity assumption for our study, we ran simulations with CESM 1.2[47] that mirrored the GeoMIP experiments and also included an experiment that offset half the radiative forcing from the $4\times CO_2$ experiment. Supplementary Table 4 reproduces Table 1 for the simulated and linearly scaled half-SG case for CESM 1.2. The results are broadly similar, but the areas reported differ by a few percent. The linearly scaled GeoMIP half-SG results should thus provide a reasonable estimate of the half-SG response that would be simulated.

Variables. We evaluate annual-mean surface (2 m) air temperature (T) and annual-mean precipitation minus evaporation (PE) for all models. We also evaluate two indices of daily extremes from the Expert Team on Climate Change Detection and Indices:[48] maximum annual surface air temperature (TXx referred to here as Tx) and maximum annual 5-day precipitation (Rx5day, referred to here as Px). These extreme indices were available for only 8 of the 12 GeoMIP models (see Supplementary Table 5). These extreme indices data were the same as used in Curry et al.[28]. These extreme indices were regridded to a median model grid resolution of 144×96 (2.5° longitude×1.9° latitude), which corresponds to the grid of the NorESM1-M model. A first-order conservative remapping algorithm was used[49], carried out using the Climate Data Operators package (CDO, http://code.zmaw.de/projects/cdo).

We include both T and Tx as T is a good predictor of general climate regime shifts and Tx is a good indicator for extreme heat risk. We focus on annual-mean PE as an indicator of overall changes to long-run water availability and exclude precipitation from our analysis in the main text as it does not capture the substantial changes in evapotranspiration expected due to the direct physiological effect of CO_2 on plants and the reduced surface energy availability that results from reduced insolation at the surface[19,50]. Px is a good predictor of changes in large-scale flooding events such as those accompanying Hurricane Harvey[51]. We do not address sea-level rise in this study but all indications are that SG would reduce global sea-level rise, although its efficacy is uncertain[52,53].

We also evaluate the global mean of the tropical cyclone power dissipation index (PDI) for the HiFLOR model, where PDI is calculated as in equation (2).

$$PDI \equiv \int_0^\tau V_{max}^3 dt \qquad (2)$$

where V_{max} is the maximum sustained wind speed at 10 m and the integral is over τ, the lifetime of the storm[27]. PDI gives an approximation to the total power dissipation of a tropical storm and is an indication of the total threat posed by the storm.

Together, these variables cover most of the drivers of the key risks of climate change identified by the IPCC AR5 WG2. Supplementary Table 3 from this report lists the physical hazards and vulnerabilities that combine to create these key risks. Supplementary Table 1 compares the physical hazards listed in that table with the five variables analysed here and shows that together they cover most of the drivers of these key hazards.

Weightings and masks. *Land area without Greenland and Antarctica.* Bounding boxes for Greenland and Antarctica were defined and for GFDL the fraction of land in each was set to zero. The Antarctic definition included all land below 60° S and the Greenland definition was defined as a polygon with corners at the following coordinates:

−73.5° E, 78.8° N; −73.5° E, 74.5° N; −44.5° E, 57.5° N; −10° E, 73.5° N; −10° E, 84.5° N; −37.5° E, 84.5° N; −60.5° E, 82.5° N

For GeoMIP, the high-resolution GFDL bounding box was regridded to each model's grid using the distance-weighted average regridding routine of CDO and used to adjust down the fraction of land in each gridcell.

Population weighting. We employed the GPWv4 gridded population dataset to create a count of population in each model gridcell[54]. For each gridcell we summed all gridded GPWv4 population counts whose centroid was in the gridcell boundaries.

Statistical test for exacerbation and moderation. We defined a region as exacerbated when the half-SG anomaly has a greater absolute magnitude than the $2\times CO_2$ anomaly. We tested for statistical significance by first running a 90% t-test using the absolute anomalies and the standard deviations of half-SG and $2\times CO_2$. Two additional 90% t-tests were run to determine whether $2\times CO_2$ and half-SG were each statistically significantly different from the control. If the absolute anomalies were significantly different but both $2\times CO_2$ and half-SG are not significantly different from the control, then we counted the statistical test as failed. In the case that the absolute anomalies were significantly different but one other test was failed, there were two options: (1) if $2\times CO_2$ was not significantly different from the control and half-SG was, then the region must report an exacerbation, and (2) if $2\times CO_2$ was significantly different from the control and half-SG was not, then the region must report a moderation. As our analysis focused on changes in annual-mean climate, the sample size for the t-test was defined as equal to the number of years in the averaging period; that is, 100 years for HiFLOR and 40 years for the GeoMIP models. In the regional analysis, the regional mean was taken before the standard deviation was calculated.

Regional analysis. We used the IPCC SREX region definitions for Fig. 3[55]. These region definitions were used to create masks on the GFDL HiFLOR grid. These high-resolution masks were then regridded to each GeoMIP model grid using the distance-weighted average regridding routine of CDO. For each variable, the land-area mean of each regional mask was taken to produce annual-average timeseries. From these timeseries, the mean and standard deviation for the evaluation period were calculated.

Data availability
The GeoMIP and CMIP5 data used in this study are available on the Earth System Grid (https://www.earthsystemgrid.org/), the processed HiFLOR data used in this study will be made available upon request.

References
35. Jia, L. et al. Improved seasonal prediction of temperature and precipitation over land in a high-resolution GFDL climate model. *J. Clim.* **28**, 2044–2062 (2014).
36. Delworth, T. L. et al. Simulated climate and climate change in the GFDL CM2.5 high-resolution coupled climate model. *J. Clim.* **25**, 2755–2781 (2012).
37. Delworth, T. L. et al. GFDL's CM2 global coupled climate models. part I: formulation and simulation characteristics. *J. Clim.* **19**, 643–674 (2006).
38. Gnanadesikan, A. et al. GFDL's CM2 global coupled climate models. part II: the baseline ocean simulation. *J. Clim.* **19**, 675–697 (2006).
39. Wittenberg, A. T., Rosati, A., Lau, N.-C. & Ploshay, J. J. GFDL's CM2 global coupled climate models. Part III: tropical Pacific climate and ENSO. *J. Clim.* **19**, 698–722 (2006).
40. Putman, W. M. & Lin, S.-J. Finite-volume transport on various cubed-sphere grids. *J. Comput. Phys.* **227**, 55–78 (2007).
41. Murakami, H. et al. Seasonal forecasts of major hurricanes and landfalling tropical cyclones using a high-resolution gfdl coupled climate model. *J. Clim.* **29**, 7977–7989 (2016).
42. Zhang, W. et al. Improved simulation of tropical cyclone responses to enso in the western north pacific in the high-resolution GFDL HiFLOR coupled climate model. *J. Clim.* **29**, 1391–1415 (2015).
43. Taylor, K. E., Stouffer, R. J. & Meehl, G. A. An overview of CMIP5 and the experiment design. *Bull. Am. Meteorol. Soc.* **93**, 485–498 (2011).
44. Emanuel, K., Ravela, S., Vivant, E. & Risi, C. A statistical deterministic approach to hurricane risk assessment. *Bull. Am. Meteorol. Soc.* **87**, 299–314 (2006).
45. Moreno-Cruz, J. B., Ricke, K. L. & Keith, D. W. A simple model to account for regional inequalities in the effectiveness of solar radiation management. *Clim. Change* **110**, 649–668 (2012).
46. Schaller, N., Sedláček, J. & Knutti, R. The asymmetry of the climate system's response to solar forcing changes and its implications for geoengineering scenarios. *J. Geophys. Res. Atmos.* **119**, 5171–5184 (2014).
47. Hurrell, J. W. et al. The community earth system model: a framework for collaborative research. *Bull. Am. Meteorol. Soc.* **94**, 1339–1360 (2013).
48. Karl, T. R., Nicholls, N. & Ghazi, A. in *Weather and Climate Extremes* 3–7 (Springer, Dordrecht, 1999).
49. Jones, P. W. First- and second-order conservative remapping schemes for grids in spherical coordinates. *Mon. Weather Rev.* **127**, 2204–2210 (1999).
50. Irvine, P. J. et al. Key factors governing uncertainty in the response to sunshade geoengineering from a comparison of the GeoMIP ensemble and a perturbed parameter ensemble. *J. Geophys. Res. Atmos.* **119**, 2013JD020716 (2014).
51. Oldenborgh, G. Jvan et al. Attribution of extreme rainfall from Hurricane Harvey, August 2017. *Environ. Res. Lett.* **12**, 124009 (2017).
52. Irvine, P. J., Sriver, R. L. & Keller, K. Tension between reducing sea-level rise and global warming through solar-radiation management. *Nat. Clim. Change* **2**, 97–100 (2012).
53. Irvine, P. J., Keith, D. W. & Moore, J. Brief communication: understanding solar geoengineering's potential to limit sea level rise requires attention from cryosphere experts. *Cryosphere Discuss.* **2018**, 1–15 (2018).
54. GPWv4. Documentation for the Gridded Population of the World v.4 (NASA Socioeconomic Data and Applications Center, 2016).
55. Seneviratne, S. I. et al. in *Managing the Risks of Extreme Events and Disasters to Advance Climate Change Adaptation* appendix 3.a (Intergovernmental Panel on Climate Change, 2012).